Journal of Materials Chemistry B

ROYAL SOCIETY OF CHEMISTRY

PAPER

View Article Online
View Journal | View Issue

Cite this: J. Mater. Chem. B, 2025, 13, 8195

Development of a glycine-modified iron oxide nanoparticle-electrochemical biosensor for specific detection of *Klebsiella pneumoniae* DNA†

Rutuja Prashant Gambhir,[a] Somnath Kundale,[b] Sohel B. Shaikh,[a] Amol S. Vedpathak,[c] Rajanish K. Kamat,[de] Tukaram D. Dongale,[b] Yogendra Kumar Mishra,[f] Ravindra N. Bulakhe,*[g] Ji Man Kim*[g] and Arpita Pandey Tiwari*[ah]

Received 19th February 2025,
Accepted 29th May 2025

DOI: 10.1039/d5tb00377f

rsc.li/materials-b

This study presents a simple electrochemical DNA biosensor to accurately detect *Klebsiella pneumoniae* DNA. The biosensor uses glycine functionalized iron oxide nanoparticles (glycine@Fe_3O_4) to capture *Klebsiella pneumoniae* DNA. The as-synthesized nanoparticles were characterized using X-ray diffraction, X-ray photoelectron spectroscopy, Raman spectroscopy, and transmission electron microscopy, and created a sensitive electrode surface that produced strong electrochemical signals when DNA attached. Electrochemical techniques, including cyclic voltammetry and square wave voltammetry, were used to develop a biosensor for detecting *Klebsiella pneumoniae* DNA. The biosensor showed limits of detection of 3.27 nM in the 30–90 nM range and 3.94 nM in the 120–270 nM range, with limits of quantification of 3.90 nM and 11.95 nM, respectively. The sensitivity, determined from calibration curves, was 0.1009 μA nM^{-1} for the low range and 0.0838 μA nM^{-1} for the high range. The biosensor demonstrated high sensitivity and selectivity, effectively distinguishing the analyte from interferents like albumin and folic acid. Molecular docking showed strong DNA binding (−6 kcal mol^{-1}). Lab tests confirmed detection of *Klebsiella pneumoniae* antimicrobial resistance genes (SHV, TEM, CTX-M, OXA-1) *via* PCR-based gel electrophoresis. This easy-to-use non-enzymatic biosensor offers fast, accurate, rapid, sensitive, and specific *Klebsiella pneumoniae* DNA detection, valuable for point-of-care diagnostics and antimicrobial resistance monitoring.

1. Introduction

Hospital-borne infections, particularly those caused by *Klebsiella pneumoniae (K. pneumoniae)*, are a significant threat within healthcare settings. *K. pneumoniae* is a Gram-negative bacterium known for its high virulence and antimicrobial resistance, making it a leading cause of severe infections in these environments. Traditional methods of detecting *K. pneumoniae* rely on lengthy culturing processes and the use of specialized equipment. These methods are time-consuming, which highlights the urgent need for faster and more sensitive detection techniques. Electrochemical DNA sensing has emerged as a promising solution for rapid and specific pathogen detection.[1–5] The primary objective of this study was to present an electrochemical DNA sensing platform specifically designed for the detection of *K. pneumoniae* DNA. This was achieved by using glycine-functionalized magnetic nanoparticles (glycine@Fe_3O_4). Magnetic nanoparticles enhance the sensitivity of the biosensor by improving the capture and separation of target DNA, thereby easing more efficient detection.[6–8] The sensing process involves two key

[a] Department of Medical Biotechnology and Stem Cells and Regenerative Medicine, Centre for Interdisciplinary Research, D. Y. Patil Education Society (Deemed to be University), Kolhapur, Maharashtra, 416006, India. E-mail: arpitaptiwari@gmail.com
[b] School of Nanoscience and Biotechnology, Shivaji University, Kolhapur, Maharashtra, 416004, India
[c] Symbiosis Centre for Nanoscience and Nanotechnology (SCNN), Symbiosis International (Deemed University), Lavale, Pune, 412115, India
[d] Department of Electronics, Shivaji University, Kolhapur 416004, India
[e] Dr Homi Bhabha State University, 15, Madam Cama Road, Mumbai 400032, India
[f] Smart Materials, Nano SYD, Mads Clausen Institute, University of Southern Denmark, Alsion 2, Sønderborg 6400, Denmark
[g] Department of Chemistry, Sungkyunkwan University, Suwon, 16419, Republic of Korea. E-mail: bulakhe@skku.edu, jimankim@skku.edu
[h] Global Innovative Center of Advanced Nanomaterials, College of Engineering, Science and Environment, University of Newcastle, Callaghan, NSW, 2308, Australia

† Electronic supplementary information (ESI) available. See DOI: https://doi.org/10.1039/d5tb00377f

steps: capturing the target DNA and amplifying the signal, which results in increased sensitivity and reduced assay time.[9–11] This approach is particularly important since *K. pneumoniae* DNA is often present in extremely low quantities in clinical samples, presenting significant analytical challenges.[12,13]

A major concern with *K. pneumoniae* infections is the presence of genes associated with multidrug resistance, such as *Sulphydryl Variable* (SHV), *Temoniera* (TEM), *Cefotaxime-Munich* (CTX-M), *Oxacillinase* (OXA), and *CMY AmpC β-lactamase* (CMY). The detection of these resistance genes is key for understanding and controlling the spread of resistant strains. The developed electrochemical DNA sensing platform offers a label-free detection method, eliminating the need for additional probe DNA or hybridizing enzymes, which simplifies the detection process.

To assess the performance of this sensor, clinical samples were analysed and the results compared to traditional techniques. The electrochemical DNA sensing platform demonstrated significant promise for rapid diagnosis, surveillance, and monitoring of *K. pneumoniae* infections in healthcare settings. By enabling quicker detection, it can facilitate the timely administration of appropriate antibiotics, thereby reducing the risk of severe infections and improving patient outcomes.

Electrochemical techniques, such as cyclic voltammetry (CV), square wave voltammetry (SWV) and electrochemical impedance spectroscopy (EIS), are commonly used for DNA sensing. Among these, EIS is particularly effective for analysing bio-recognition processes at the electrode surface, such as nucleic acid interactions.[14–16] EIS-based biosensors are known for their low cost, quick reaction times, and potential for miniaturization, making them ideal for real-time, label-free DNA detection with minimal sample preparation.[17–21]

In conclusion, this study advances the field of electrochemical DNA sensing by introducing a non-enzymatic adsorption mechanism. As summarized in Table 1, our findings exhibit high specificity and competitive sensitivity for DNA detection (0–300 nM) using CV, EIS, and SWV techniques, while utilizing fewer chemical components compared to other electrochemical biosensors reported between 2020 and 2025. The platform developed in this research provides a valuable tool for detecting and monitoring *K. pneumoniae* infections and holds promise for future applications in detecting other pathogenic bacteria as well.

2. Materials and methods

Analytical grade (AR grade 99.9%) phosphate buffer saline solution (PBS), sodium hydroxide (NaOH), glycine ($C_2H_5NO_2$), ferric ($FeCl_2{\cdot}4H_2O$), and ferrous ($FeCl_3{\cdot}6H_2O$) chloride were purchased from Himedia Pvt. Ltd. They were used directly without additional purification after purchase. Double distilled water (DDW) was incorporated for subsequent reactions. An electrochemical workstation (Biologic VSP) was used for all electrochemical measurements. Scanning electron microscopy (SEM, JSM-7900F, JEOL, Japan), X-ray photoelectron spectroscopy (XPS, K alpha plus), transmission electron microscopy (TEM, JEM-2010, JEOL, Japan. 200 kV), and Raman spectroscopy (Model: Flex G, Tokyo Instruments) were performed in this work.

2.1. Synthesis of glycine@Fe_3O_4 nanoparticles

The glycine@Fe_3O_4 nanoparticles were synthesized with a co-precipitation method as reported earlier.[37] The resulting magnetic nanoparticles were characterized using various analytical techniques such as X-ray diffraction (XRD), scanning electron microscopy (SEM), transmission electron microscopy (TEM), X-ray photoelectron spectroscopy (XPS), and Raman spectroscopy to determine their size, crystalline structure, and morphology.

2.2. Glycine@Fe_3O_4–DNA conjugation

K. pneumoniae DNA containing clinical samples were obtained from D. Y. Patil Hospital, Kolhapur, MS, India. DNA quantification and polymerase chain reaction PCR-associated agarose gel electrophoresis were performed to evaluate the DNA sensing efficiency. DNA–glycine@Fe_3O_4 interactions were optimized

Table 1 Comprehensive comparison of recent advancements in electrochemical biosensors from 2020 to 2025

No.	Detection range	Detection molecule	Probe used	Specificity	Electrochemical methods	Electrolyte used	Number of chemicals used	Ref.
1	10–500 nM	Cancer biomarkers	Yes, aptamer-based	High	Cyclic voltammetry (CV), EIS	PBS (pH 7.4)	5	22
2	5–200 nM	Glycoproteins	No	Moderate	Differential pulse voltammetry (DPV)	0.1 M PBS	4	23
3	1–100 nM	DNA	Yes, DNA probe	High	Square wave voltammetry (SWV)	1 M PBS	6	24
4	50 nM–1 μM	Proteins	No	Moderate	Linear sweep voltammetry (LSV)	0.5 M NaCl	3	25
5	2–50 nM	RNA	Yes, RNA probe	High	CV, EIS	0.1 M PBS	7	26
6	10–100 μM	Glucose	No	Low	Amperometry	0.1 M KCl	2	27
7	1–10 μM	Heavy metals	No	Moderate	DPV	0.1 M HCl	4	28
8	5–500 nM	miRNA	Yes, miRNA probe	High	CV, SWV	1 M PBS	6	29
9	10 nM–1 μM	Pathogens	Yes, antibody-based	High	EIS	0.1 M PBS	5	30
10	100 nM–10 μM	Enzymes	No	Low	CV	0.1 M NaOH	3	31
11	1–100 nM	DNA	Yes, aptamer-based	High	DPV, EIS	0.5 M PBS	8	32
12	10–100 μM	Environmental toxins	No	Moderate	Amperometry	0.1 M NaCl	4	33
13	5–200 nM	COVID-19 antigens	Yes, antibody-based	High	CV, DPV	1 M PBS	6	34
14	50 nM–1 μM	Biomolecules	No	Moderate	SWV	0.1 M PBS	5	35
15	1–10 μM	Enzymes	No	Low	CV	0.1 M NaOH	3	36
16	0 – 300 nm	DNA	No	High	CV, EIS, SWV	1 M PBS	4	Our findings

using the following parameters: concentration of DNA, pH of the electrolyte, and incubation time. A detailed description is provided in the ESI.†

2.3. Fabrication of the biosensor

2.3.1. Fabrication of glycine@Fe_3O_4–GCE. The GCE was modified using glycine@Fe_3O_4 with the drop cast method. These nanoparticles were then dispersed in PBS (1 M) to form a homogeneous suspension. Subsequently, the GCE was submerged in the suspension, allowing nanoparticles to adhere to its surface by drop casting. Afterward, the modified electrode was left to dry at room temperature overnight, ensuring firm attachment of nanoparticles to the electrode. The resulting modified electrode exhibited improved magnetic and electrochemical properties, rendering it suitable for DNA sensing.

2.3.2. Electrochemical measurements. A three-electrode cell system in 1 M PBS pH 5 electrolyte was used to conduct electrochemical DNA sensing analysis of the glycine@Fe_3O_4 nanoparticle-modified glassy carbon electrode glycine@Fe_3O_4–GCE. Ag/AgCl, platinum wire, and glycine@Fe_3O_4–GCE were used as reference, counter, and working electrodes, respectively. The working electrode glycine@Fe_3O_4–GCE was first stabilized for a limited number of cyclic voltammogram (CV) cycles in 1 M PBS electrolyte within a potential window of 0.2 to −0.7 V at different scan rates (10–200 mV s^{-1}) until a steady state of the voltammogram was attained. By gradually adding various (or identical) DNA concentrations in 1 M PBS at a fixed 0.5 V *versus* Ag/AgCl potential, the electrochemical properties of DNA sensing were investigated. The electrolyte 1 M PBS was continually swirled at 250 rpm to reduce mass transfer interference. By monitoring CV at various scan rates, it was possible to ascertain the nature of the redox reaction occurring with the GCE electrode. EIS, SWV, and DPV measurements were performed for DNA detection after DNA samples were introduced to the electrolyte.

2.4. Computational analysis

Interactions between *K. pneumoniae* DNA and glycine molecules present on glycine@Fe_3O_4 were studied at a computational level as a basis of primary analysis. Docking analysis was carried out with PyRX 0.8 software. The PDB structure of glycine (PDB ID-DB00145) was obtained from the protein data bank (PDB). The *K. pneumoniae* DNA model was built using Discovery studio 2021 software. Docking was performed with PyRx 0.8. Visualization of docking was done with Pymol.

3. Results and discussion

3.1. Characterization of glycine@Fe_3O_4 nanoparticles

The glycine@Fe_3O_4 nanoparticles were characterized by X-ray diffractometer (XRD), X-ray photoelectron spectroscopy (XPS), Raman spectroscopy, scanning electron microscopy (SEM), and transmission electron microscopy (TEM).

The nature of the nanoparticles was confirmed by XRD of pristine Fe_3O_4 and glycine@Fe_3O_4 with the JCPDS card value 75-0449 shown in Fig. 1a. Possibly, hydrogen bonding occurred between 2 glycine and 1 Fe_3O_4 molecules by eliminating a water molecule.

Raman spectroscopy analysis depicted alterations in composition, internal structures, and bonding as shown in Fig. 1b. Although there was no distinguishable change in the morphology of the pristine or composite materials, significant alterations at compositional and functional levels in the composite compared with pristine materials were observed. The given exciting wavelength was 532 nm with a power of 25 mW. The time of laser exposure was 5 minutes. It remained the same for all spectra. Pristine Fe_3O_4 had a characteristic peak near 670 nm as shown in Fig. 1b, which confirmed the magnetite phase of the synthesized material (Fe_3O_4).[38] The absence of other peaks depicted that Fe_3O_4 was a poor Raman scatterer. Pristine glycine indicated a Raman scattering effect in a wide range with the presence of NH, OH, and CH_2 stretching as shown in Fig. 1b. Peaks above 2000 cm^{-1} (3007, 2972, 2806, and 2595 cm^{-1}) depicted NH and OH-stretchings. The peak at 1576 cm^{-1} represented distorted carbon. The peaks at 1412, 1320, 1143, 1033, and 899 cm^{-1} represented CH_2 stretchings, whereas the peaks at 700, 604, 501, 369, 200, 120, and 82 cm^{-1} indicated interactions between water molecules (solvent) and outer surface atoms of glycine molecules.[39] As shown in Fig. 1b, the peak at 2146 cm^{-1} depicted OH-stretching. The peak at 1318 cm^{-1} showed CH_2 stretching. Peaks at 672 and 613 cm^{-1} depicted the presence of Fe_3O_4. Some traces of Fe_2O_3 were also present in the composite sample based on peaks located at 404, 305, and 232 cm^{-1} in the spectrum. The Glycine@Fe_3O_4 composite showed a clear red shift, signifying that light scattering shifted to lower wavelengths as shown in Fig. 1b. Hence, it could be interpreted that the formation of glycine@Fe_3O_4 could change the light-scattering properties of the pristine material. Raman analysis showed the non-elastic nature of the collisions between the light particles and glycine@Fe_3O_4. As a property of a non-elastic collision, colliding light particles will either gain or emit electromagnetic radiation from the collided matter, here glycine@Fe_3O_4. Here, a red shift was observed for glycine@Fe_3O_4. When wavelength shift occurs from higher to lower, it is called a Raman redshift. The Raman spectrum provides the basis of bond vibrations. The spectra revealed the main phase of the nanomaterial, *i.e.*, magnetite Fe_3O_4. Changes in Raman spectra of glycine@Fe_3O_4 acted as a function of doping or surface modification to the pristine Fe_3O_4. These obtained peaks were material-specific. The advantage of characterizing particles using Raman spectroscopy is that the composition of amino acids such as glycine would not alter[40] because the analysis is carried out at room temperature. In Fig. 1(c–e), pristine Fe_3O_4 shows a hybrid morphology for the majority of particles. Also, aggregation is seen as the particles are in solution. Pristine glycine showed a smooth nearly triangular morphology, which might have acted as a base for DNA attachments. The Glycine@-Fe_3O_4 composite shows similar morphology to pristine Fe_3O_4. It can be interpreted that no morphological alteration has occurred due to the addition of glycine in Fe_3O_4. The SEM image of pristine Fe_3O_4 showed a nearly cuboidal (or hybrid) morphology for many particles. However, some particles had distorted shapes. It also

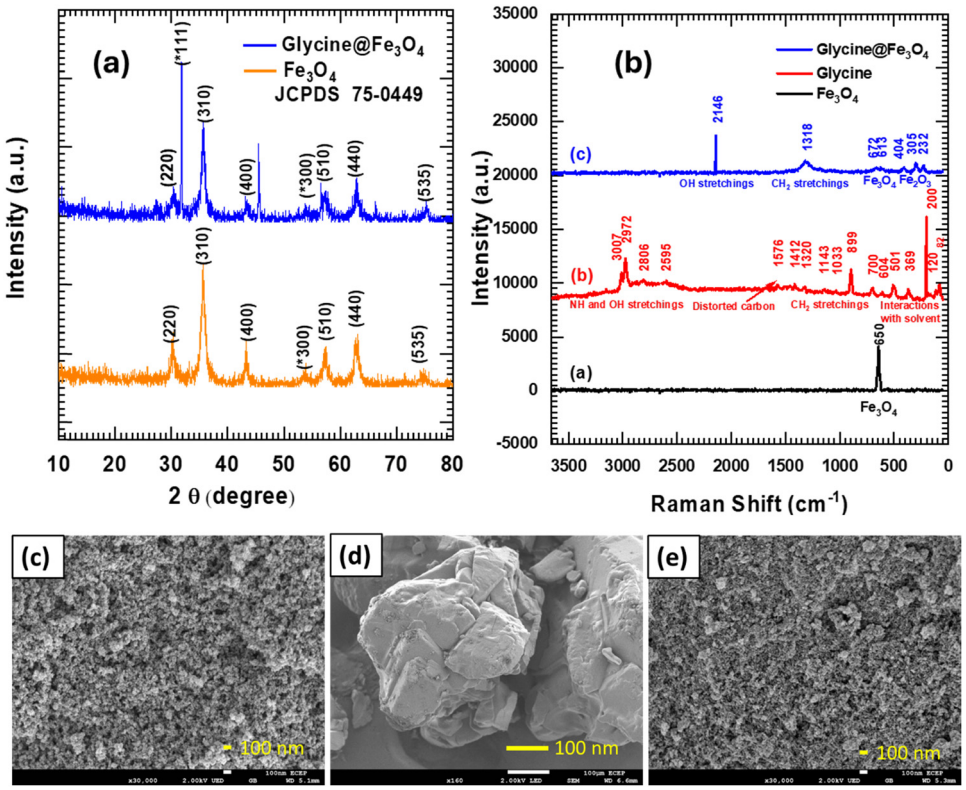

Fig. 1 Characterization of the pristine Fe_3O_4 and glycine@Fe_3O_4 nanoparticles; (a) XRD, (b) Raman, (c) SEM of pristine Fe_3O_4, (d) pristine glycine and (e) the glycine@ Fe_3O_4 composite.

revealed agglomeration of particles in a solution form. Glycine is considered the smallest and simplest amino acid with a simple carbon chain. SEM analysis showed fused triangular particles with smooth surfaces. The image of glycine@Fe_3O_4 depicted a similar morphology to pristine Fe_3O_4. Glycine modification did not affect the morphology of the particles. It could be interpreted that no morphological alteration occurred due to the addition of glycine in Fe_3O_4. The average size of glycine@Fe_3O_4 was calculated to be 16 ± 20.54 nm based on the TEM micrographs (Fig. S2, ESI†).

XPS analysis was performed to confirm the functionalization or modification of the surface of Fe_3O_4, as shown in Fig. 2a and b for pristine Fe_3O_4 and glycine@Fe_3O_4, respectively. Fig. 2a(a′) displays the Fe 2p region, showing the presence of Fe, with Fe $2p_{1/2}$ and Fe $2p_{3/2}$ peaks. In pristine Fe_3O_4, only Fe and O elements are present. In contrast, Fig. 2b(b′) highlights the glycine@Fe_3O_4 sample, which also displays Fe 2p peaks, along with the presence of nitrogen, indicating the successful incorporation of glycine. Additionally, Fig. 2a(a″) and b(b″) shows the O 1s peak, confirming the presence of oxygen in both the modified and unmodified samples.

Therefore, from all the above characterizations, it was concluded that the synthesized nanoparticles are glycine-modified iron oxide nanoparticles glycine@Fe_3O_4.

3.2. Electrochemical biosensor

The three-electrode system-based electrochemical biosensor was employed to detect *K. pneumoniae* DNA based on the abovementioned optimized parameters. Previously, in pilot experiments, a 1 : 1 glycine@Fe_3O_4 nanoparticle : DNA ratio provided the best optimum results for the conjugation (Fig. S3–S5, ESI†). However, to improve the ease of application and achieve a wider detection range, the 100 μg mL^{-1} glycine@Fe_3O_4 nanoparticles were drop cast onto the working electrode. To determine if the biosensor detects smaller DNA quantities, its efficiency was analyzed in nanomolar ranges for early-stage disease detection.

3.3. Electrochemical analysis of the developed biosensor with CV, EIS, and SWV

The following are the techniques used to study the efficiency of the proposed biosensor.

3.3.1. Cyclic voltammetry study (CV). Fig. 3 depicts a cyclic voltammogram of glycine@Fe_3O_4–GCE electrochemically sensed at various scan rates of standard DNA in PBS (1 M) electrolyte. The electrochemical activity of the glycine@Fe_3O_4–GCE was studied by cyclic voltammetry (CV) within the potential range of 0.2 to −0.7 V. These experiments were carried out at different scan rates between 10 and 200 mV s^{-1} in a typical supporting electrolyte in 1 M phosphate-buffered saline PBS. A well-defined pair of redox peaks was observed, indicating a reversible electrochemical process at the electrode surface. Interestingly, the peak current was linearly increased with the square root of the scan rate, indicating a diffusion-controlled electron transfer mechanism. Such behavior proves the successful surface functionalization by glycine, which

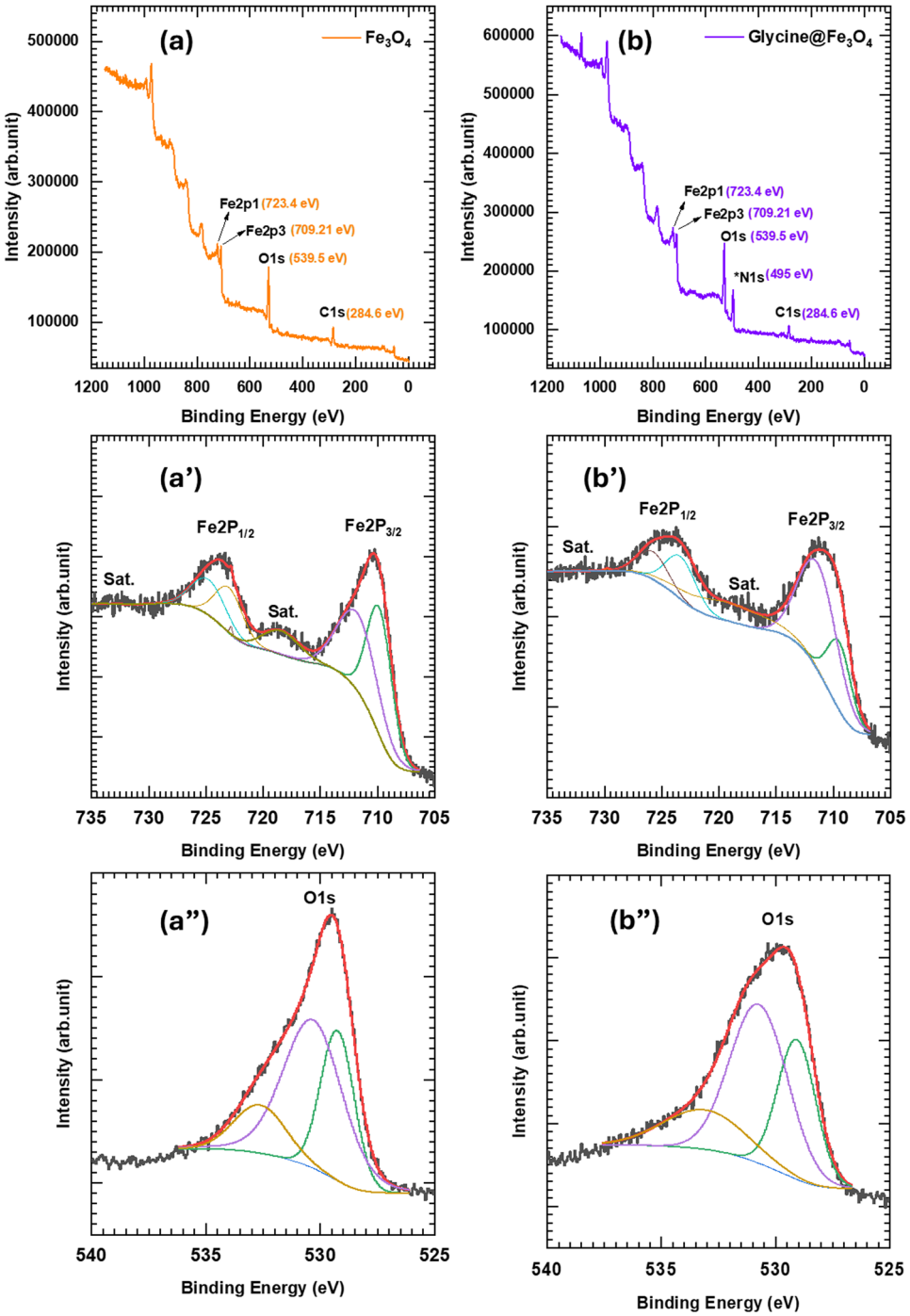

Fig. 2 Characterization of pristine Fe_3O_4 and glycine@Fe_3O_4 nanoparticles; (a), (a′) and (a″) XPS of pristine Fe_3O_4; and (b), (b′) and (b″) glycine@Fe_3O_4.

increases the conductivity and favors rapid electron exchange between the modified electrode and the electrolyte.

Fig. 4 shows the cyclic voltammetry (CV) curves of the glycine@Fe_3O_4-modified electrodes in the presence of DNA at concentrations ranging from 0 to 300 nM, recorded at scan rates of (a) 20 mV s^{-1}, (b) 40 mV s^{-1}, and (c) 60 mV s^{-1}. As the DNA concentration increases, a gradual change in the redox peak currents is observed, indicating effective interaction between the DNA molecules and the modified electrode surface. Fig. 4(d) presents the electrochemical impedance spectroscopy (EIS) data for the glycine@Fe_3O_4-modified electrode at 60 mV s^{-1} following exposure to varying DNA concentrations. The Nyquist plots reveal a systematic change in the charge transfer resistance (R_{ct}), confirming the successful immobilization and surface binding of DNA onto the electrode.

3.3.2. Electrochemical Impedance Spectroscopy study (EIS). Furthermore, to study the significant distinction of electrochemical responses between glycine@Fe_3O_4 and DNA at the working

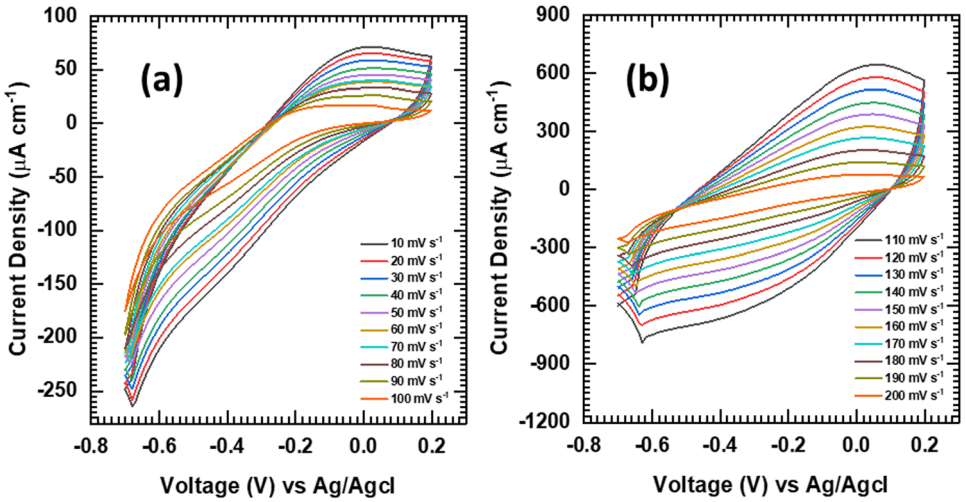

Fig. 3 Cyclic voltammetry curves of glycine@Fe_3O_4–GCE electrochemically studied at various scan rates of standard DNA in PBS (1 M) electrolyte; (a) 10–100 mV s^{-1}, and (b) 110–200 mV s^{-1}.

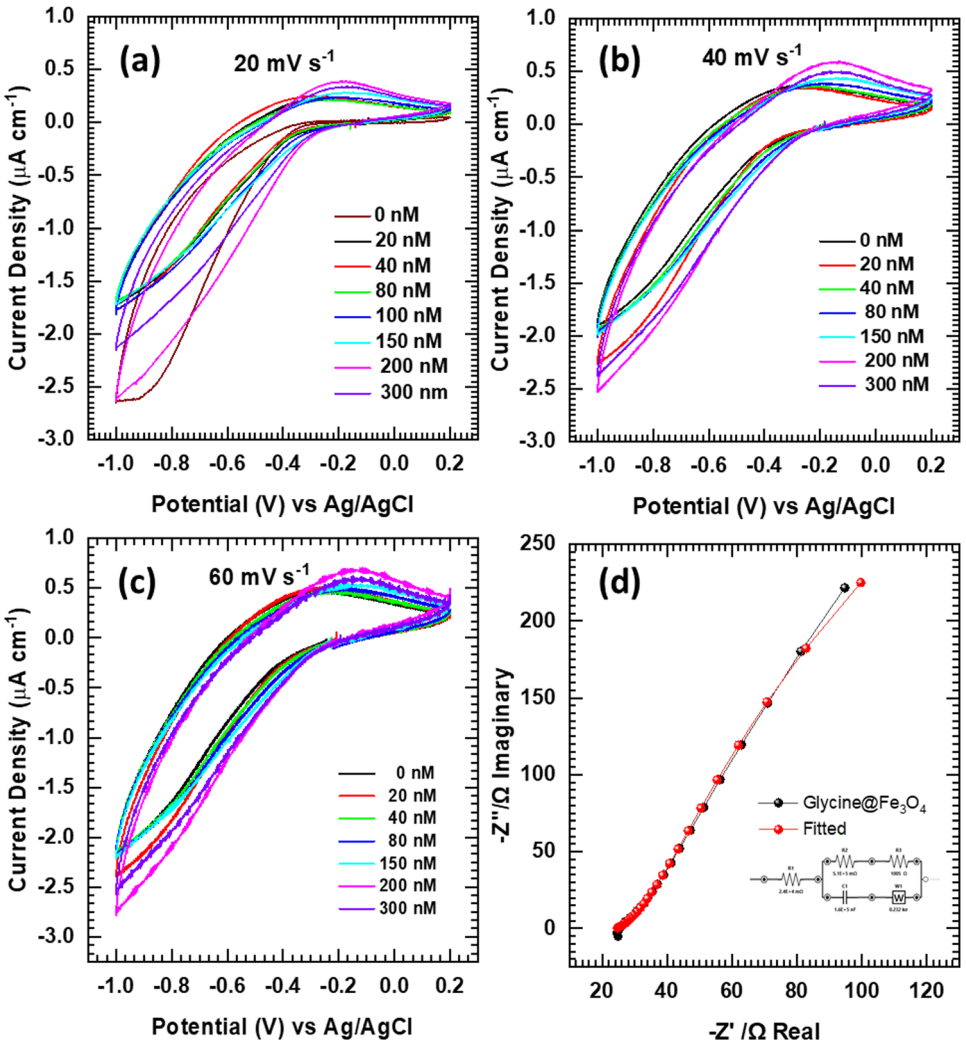

Fig. 4 Cyclic voltammetry curves of glycine@Fe_3O_4-modified electrodes with DNA at concentrations ranging from 0 to 300 nM at scan rates of (a) 20 mV s^{-1}, (b) 40 mV s^{-1}, and (c) 60 mV s^{-1}. (d) EIS of the 60 mV s^{-1} glycine@Fe_3O_4 modified electrode after treatment with 0 to 300 nM DNA concentrations.

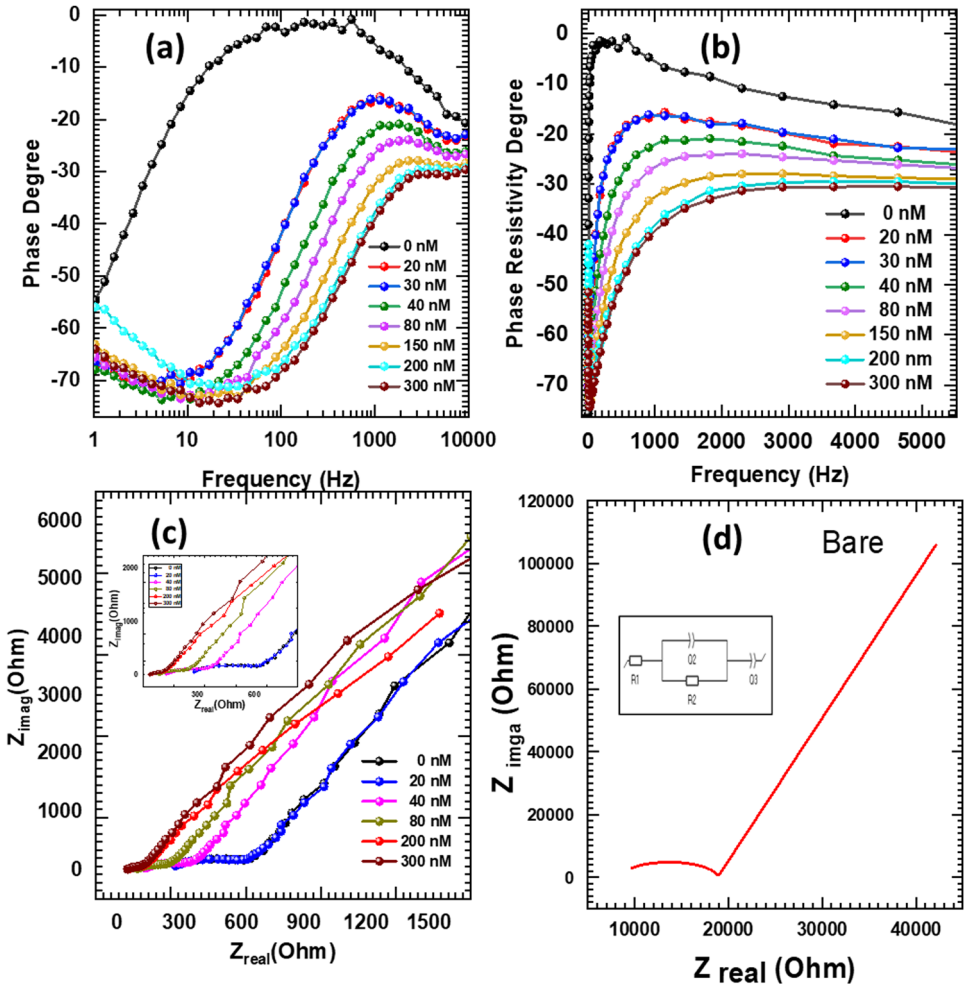

Fig. 5 Electrochemical impedance spectrometry (EIS) responses of glycine@Fe_3O_4-based DNA sensing with DNA at concentrations ranging from 0 to 300 nM. (a) Bode plot, (b) phase resistivity spectrum, and (c) and (d) Nyquist plots showing significant concentration-dependent DNA sensing.

electrode surface, we used an electrochemical impedimetric approach to examine *K. pneumoniae* DNA detection. With this approach, we measured impedance over a frequency range of 10 mHz to 100 KHz. Fig. 5a depicts Bode plots of *K. pneumoniae* DNA at a concentration of 0 to 300 nM in 1 M PBS electrolyte. Bode plots showed significant variations in peak position frequency (shifted towards higher frequency) with increasing DNA concentration. For better analysis, we plotted a frequency *vs.* phase resistivity degree graph as shown in Fig. 5b. This graph significantly distinguished various concentrations of DNA. It was observed that the phase resistivity degree was directly proportional to the interaction between DNA and glycine@Fe_3O_4–GCE. A decrease in phase resistivity degree was found when the DNA content was increased.

For further investigation, we used a Nyquist plot frequently employed for impedimetric detection. Fig. 5c and d show Nyquist plots for DNA concentrations from 0 nM (bare) to 300 nM. The corresponding equivalent circuit is depicted in Fig. 5d. The equivalent circuit consisted of solution resistance (R_s) in series with a parallel combination of constant phase element (Q_2), which represents charge transfer processes at the electrode-solution interface, charge transfer resistance (R_{ct}), and constant phase element (Q_3), with interpretations for additional interactions within the system, such as diffusion effects.

Values of circuit elements for bare DNA to 300 nM DNA are shown in Table 2. Values of solution resistance (R_s) decreased from 8480 Ω to 47.9 Ω with an increase in DNA concentration, suggesting an increase of electrolyte conductivity. The curvature of the semicircle, which was correlated with the charge transfer resistance (R_{ct}), was decreased from 10 374 to 48 as DNA content increased, indicating that the electrode (glycine@Fe_3O_4) was interacting with DNA more when the DNA content was higher.[41] The value of α parameter for CPE indicates the dominance of a capacitive or resistive effect within an electrochemical cell. The value of α is 0 for pure resistive behavior. It is 1 for optimum capacitive behavior. All values for $Q2$ and $Q3$ were above 0.75, indicating that the capacitive effect was dominant at lower frequencies.[42]

3.3.3. Square wave voltammetry (SWV) analysis of *K. pneumoniae* DNA. For further analysis of the biosensing ability of the electrode, SWV analyses were carried out in a potential

Table 2 Values of circuit elements for *K. pneumoniae* DNA sensing

Sample	R_s (Ω)	Q_2 (F s^{-1})	α_2	R_{ct} (Ω)	Q_3 (F s^{-1})	α_3
Bare	8480	3.499×10^{-6}	0.9498	10 372	5.036×10^{-6}	0.8623
20 nM DNA	263	0.1489×10^{-6}	0.9546	343.8	6.08×10^{-6}	0.8345
30 nM DNA	263	0.1508×10^{-6}	0.9544	322.7	6.698×10^{-6}	0.8144
40 nM DNA	133.7	0.2944×10^{-6}	0.9272	191.2	6.715×10^{-6}	0.8153
80 nM DNA	95.04	0.4164×10^{-6}	0.9270	121.2	7.397×10^{-6}	0.8024
150 nM DNA	68.23	0.3201×10^{-6}	1	68.7	8.285×10^{-6}	0.7873
200 nM DNA	50.59	0.3734×10^{-6}	1	40.7	10.19×10^{-6}	0.7560
300 nM DNA	47.9	0.589×10^{-6}	0.9598	48.0	7.627×10^{-6}	0.8004

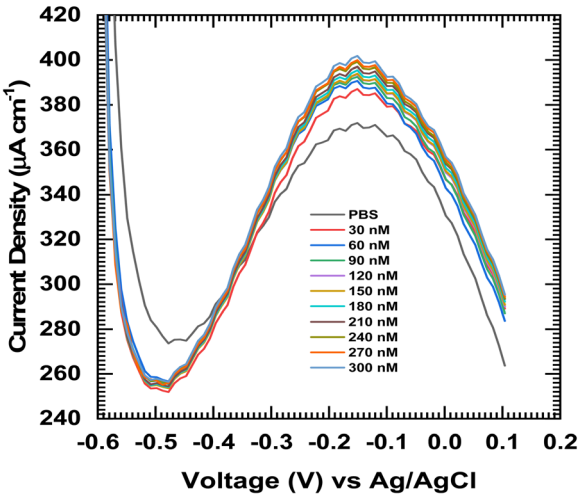

Fig. 6 Biosensing using SWV analysis with *K. pneumoniae* DNA.

window of 0.1 to −0.6 V. As shown in Fig. 6, the SWV method provides more sensitive resolution than CV and is thus suited for DNA detection. The experiments were conducted at a constant frequency of 20 Hz. After hybridization of the target DNA on the modified electrode surface, clear changes in peak current were observed. DNA generally caused larger shifts because of its stable double-helix conformation and strong interaction with the modified electrode. This response verified the specific identification and effective hybridization of complementary DNA strands, confirming the selectivity and nucleic acid detection capability of the biosensor.

3.3.4. Selectivity response of the glycine@Fe_3O_4 electrode. To confirm the selectivity of the glycine@Fe_3O_4–GCE for *K. pneumoniae* DNA, we performed the same electrochemical sensing experiments with CV and EIS (Bode plot) in the presence of different biological entities such as whole cell, protein, and bioanalyte. Fig. 7 depicts cyclic voltammograms (Fig. 7a–c) and Bode plots (Fig. 7a′, b′, and c′) for the whole cell, protein, and bioanalyte with DNA at concentrations of 0, 100, 200, and 300 nm and a scan rate of 20 mV s^{-1}. The results indicated minimal electrochemical interactions of other biomolecules (*viz.* whole cell, protein, and bioanalyte) with glycine@Fe_3O_4 not showing any significant change or variation in peak current or peak position frequency in CV or Bode plots. This suggests that glycine@Fe_3O_4 has a high selectivity toward *K. pneumoniae* DNA present in a culture.

3.3.5. Sensitivity graph and potential dependent response. For a quantitative evaluation of the sensor's performance, a sensitivity study was performed in Fig. 8 by measuring the current response at an applied potential of 0.2 V, which was found to be the best sensing voltage. Calibration curves for DNA in 1 M PBS solution over a 30 to 300 nM concentration range were made. Fig. 8a shows that the use of a 1 M PBS concentration enhances the ionic strength. This improvement in ionic strength provides better electrochemical signal stability, reduces baseline noise, and improves the reproducibility of the results. Increasing the DNA concentration gave a continually rising current for DNA with a linear response in designated ranges. The calibration plots provide essential information concerning the dynamic range and detection performance of the sensor. The linear range was recorded at two linear intervals: one for 30 to 90 nM and a second one for 120 to 270 nM. This experiment based on the potential indicated the response of the modified electrode surface with high sensitivity as well as regularity over the wide concentration interval.

3.3.6. Limit of detection (LOD), limit of quantification (LOQ), and linearity. The LOD and LOQ were determined from the calibration curves using the following standard formulas:

$$\text{LOD} = (3.3 \times \text{SD})/\text{slope} \quad (1)$$

$$\text{LOQ} = (10 \times \text{SD})/\text{slope} \quad (2)$$

As presented in Fig. 8b, the LOD and LOQ values were calculated. For DNA, for the range 30–90 nM, LOD = 3.27 nM, R^2 = 0.9972, LOQ = 3.90 nM. For the higher range of 120–270 nM, LOD = 3.94 nM, R^2 = 0.9992, and LOQ = 11.95 nM. These values emphasize the precision and accuracy of the sensor at both low and moderate levels of concentration, which reflects quick and sensitive surface hybridization. The values of LOQ dynamic range of 0–300 nM achieved by our biosensor align well with sensitivity targets commonly required in molecular diagnostics.[43–46] However, clinical standards often vary depending on the specific application and assay type. These features make the biosensor suitable for point-of-care applications and resource-limited settings. To further validate its clinical relevance, comparative testing with patient-derived samples and established diagnostic methods would be a valuable future step. Sensitivity was calculated from the slope of the calibration curves obtained at 0.2 V using the formula:

$$\text{Slope} = (3.3 \times \text{SD})/\text{LOD} \quad (3)$$

For DNA (30–90 nM) range, = 0.1009 μA nM^{-1}
For DNA (120–270 nM) range, = 0.0838 μA nM^{-1}

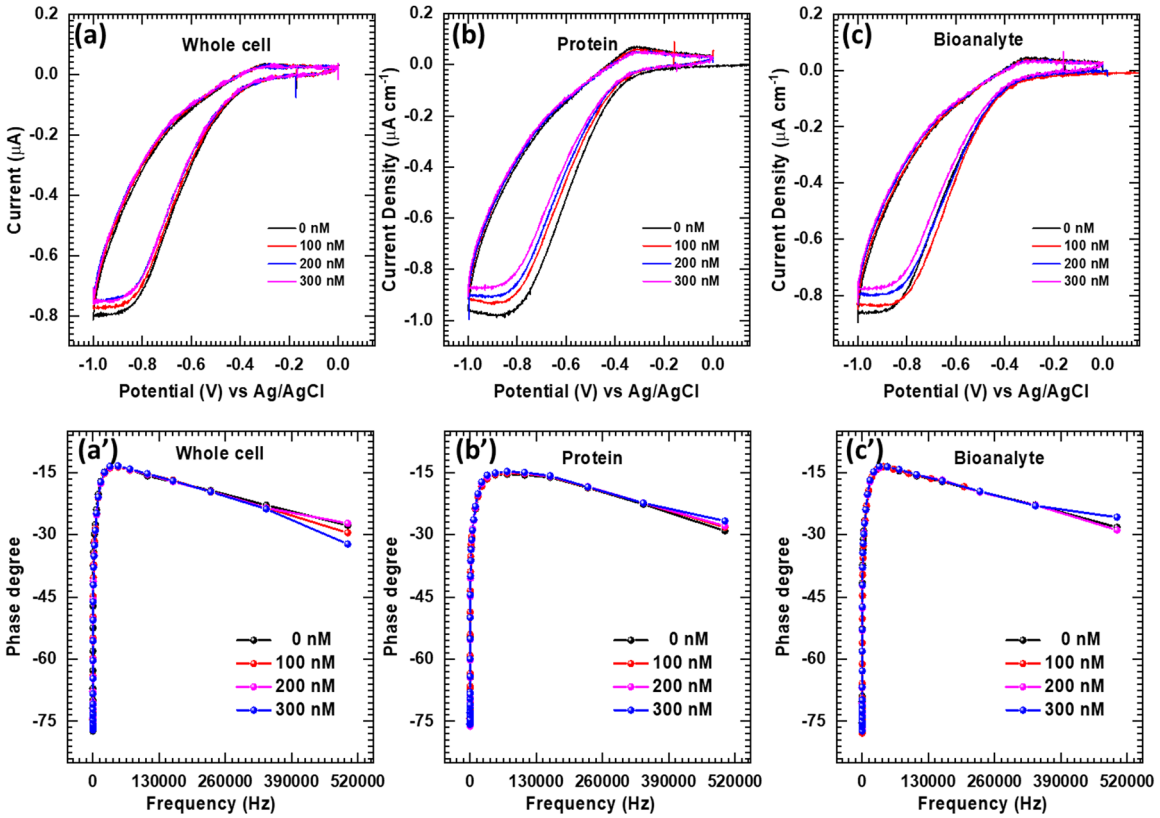

Fig. 7 (a)–(c) Cyclic voltammogram, and (a′)–(c′) EIS responses of the glycine@Fe_3O_4 electrode under successful addition of whole bacterial cells, proteins (albumin), and bioanalytes (folic acid) with concentrations ranging from 0 to 300 nM. No significant responses were obtained for these analytes.

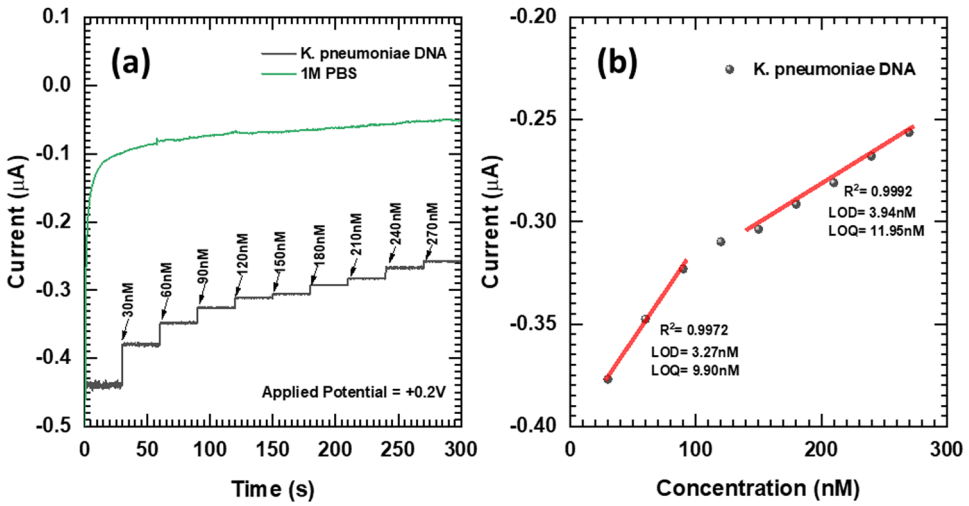

Fig. 8 (a) Sensitivity analysis of *K. pneumoniae* DNA biosensing in 1 M PBS and, (b) limit of detection and limit of quantification *K. pneumoniae* DNA.

With the working electrode surface area 0.07 cm^2 (GCE):
(1) DNA 30–90 nM (low range): 1.441 μA nM^{-1} cm^{-2}
(2) DNA 120–270 nM (high range): 1.197 μA nM^{-1} cm^{-2}

These results indicate that the sensor has greater sensitivity in DNA detection, particularly at low concentrations, which is beneficial for the detection of bacteria at early stages or trace-level nucleic acid monitoring. The glycine@Fe_3O_4 interface is providing both biocompatibility and enhanced electron transfer properties.

3.4. Analysis of the biosensor using clinical samples

Based on the Bode plot obtained in Fig. 5a, we obtained a calibration curve as shown in Fig. S6 (ESI†). Here, we considered the peak position frequency of the 0 nM Bode plot as f_i.

Table 3 Sensed anti-microbial resistant gene sequences of *K. pneumoniae* DNA

S. no.	DNA (gene)	Primer	Amplicon (bp)
1	SHV	SHV-F: CGCCTGTGTATTATCTCCCT SHV-R: CGAGTAGTCCACCAGATCCT	294
2	TEM	TEM-F: TTTCGTGTCGCCCTTATTCC TEM-R: ATCGTTGTCAGAAGTAAGTTGG	404
3	CTX-M	CTX-M-F: CGCTGTTGTTAGGAAGTGTG CTX-M-R: GGCTGGGTGAAGTAAGTGAC	754
4	OXA-1	OXA-1-F: ACACAATACATATCAACTTCGC OXA-1-R: AGTGTGTTTAGAATGGTGATC	464

Peak position frequencies for 10, 20, 40, 80, 150, 200, and 300 nM were considered as f_1–f_7, respectively. The difference between f_i and f_{1-7} was considered as Δf for each concentration. A linear fitting of the calibration plot indicated a linear increment in peak position frequency with an increase in DNA concentration (0–300 nM). For isolated unknown clinical sample concentrations, we simply measured electrochemical impedance spectroscopy (EIS) and plotted a Bode plot for it. The peak position frequency difference (Δf) was calculated by comparing with the bare peak position frequency, which was found to be, Δf = 993.13. Finally, we compared this Δf with the calibration curve and found that an isolated unknown concentration of *Klebsiella pneumoniae* DNA from the clinical culture was around 20 nM in the presence of other biomolecules in the clinical culture. The above-mentioned DNA sensing was validated with a currently used DNA detection method *i.e.*, UV-visible spectroscopy and DNA quantification, which showed an increase in DNA concentration with an increase in bacterial growth (Fig. S6c, ESI†). The sensed DNA was separated from glycine@Fe_3O_4 by ceasing the applied current, confirming that the sensed material was DNA. Conventional PCR-based agarose gel electrophoresis is shown in Fig. S6d (ESI†). Separated DNA was further PCR-amplified to detect the specific gene sequence of DNA. Qualitative PCR estimation of the sensed DNA [*K. pneumoniae*] from clinical culture was performed by 0.8% agarose gel electrophoresis. The 1st well represented a reference 100–1000 base pairs (bp) DNA ladder. The 2nd well was the SHV gene with 294 bp. The 3rd well represented the TEM gene with 404 bp. The 4th and 6th wells represented the OXA-1 gene with 464 bp. The 5th well represented the CTX-M gene with 754 bp. The 7th well represented a negative control with nuclease-free water. The obtained gene sequences in the present study are presented in Table 3.[47] Detailed conditions given for *K. pneumoniae* DNA detection are summarized in Table 4. Other PCR details are attached to the ESI.†

3.5. Mechanism of the proposed biosensor

Development of a glycine@Fe_3O_4 nanoparticle-based electrochemical biosensor for specific detection of *K. pneumoniae* DNA was carried out in six stages as given in Fig. S1 (ESI†): {1} mechanism of proposed biosensor, {2} synthesis of glycine@Fe_3O_4 nanoparticles, {3} characterization of glycine@Fe_3O_4 nanoparticles, {4} optimization of glycine@Fe_3O_4–DNA conjugation, {5} development of electrochemical biosensor, and {6} electrochemical analysis with CV, EIS, DPV, and SWV. All the stages of the study have been explained in detail below.

K. pneumoniae DNA was detected by a biosensing platform which is fabricated using glycine@Fe_3O_4 nanoparticles as shown in Scheme 1 in a stepwise manner. Initially, glycine@Fe_3O_4 nanoparticles were synthesized through the co-precipitation method and simultaneously functionalized with glycine biomolecules (Scheme 1a). Then they are immobilized on a glassy carbon electrode (GCE) using a drop casting method and it is considered as a working electrode (Scheme 1b). Two other electrodes, *viz.* counter (platinum wire) and reference (Ag/AgCl), were utilized to set up a three-electrode system as described in the methodology section.

The resulting biosensing platform when exposed to *K. pneumoniae* DNA, and the glycine@Fe_3O_4–GCE could capture the DNA present in the electrolyte, here 1 M PBS. Detection and quantification of DNA targets were achieved using suitable analytical techniques such as electrochemical measurements.

In the three electrode system, glycine@Fe_3O_4–GCE acts as an anode which possesses positive charge (+) and hence negatively charged DNA (−) attracts towards it (Scheme 1c). Glycine present on the nanoparticles achieved the actual binding to the DNA. It is an amino acid with a simple carbon chain. It conducts a positive charge on the surface and hence attracts negatively charged DNA present in the electrolyte (Scheme 1d). As a result, specific electrostatic ionic interactions take place on the electrode surface that could enable electrochemical detection of the *K. pneumoniae* DNA.[37] The above-mentioned reaction forms on the electrode surface without the addition of any enzyme or aptamers, resulting in greater selectivity towards *K. pneumoniae* DNA compared to traditional DNA sensing methods, while effectively repelling other non-specific biomolecules such as proteins and cells from the electrode surface. In contrast, the reference electrode possesses negative charge (−) and therefore negatively charged DNA (−) gets repelled by

Table 4 Given PCR conditions for *K. pneumoniae* DNA detection

Steps	TEM	SHV	CTX-M	OXA-48
Initial denaturation	94 °C for 5 min	94 °C for 5 min	94 °C for 5 min	94 °C for 3 min
Denaturation	94 °C for 30 s	94 °C for 30 s	94 °C for 30 s	61.7 °C for 5 min
Annealing	65.5 °C for 30 s	60 °C for 30 s	60 °C for 30 s	61.7 °C for 30 s
Extension	72 °C for 50 s	72 °C for 50 s	72 °C for 50 s	72 °C for 1 min
Final extension	72 °C for 5 min	72 °C for 5 min	72 °C for 5 min	72 °C for 7 min
Cycles	35	35	35	35
Hold	4 °C	4 °C	4 °C	4 °C

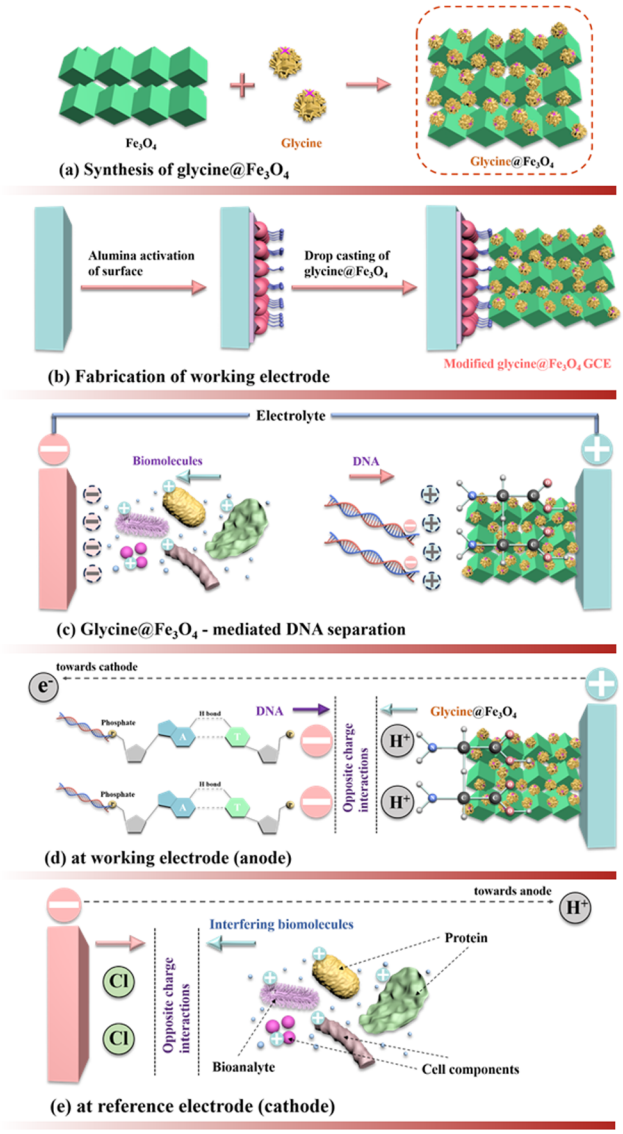

Scheme 1 DNA biosensor platform using glycine@Fe_3O_4. (a) Synthesis of glycine@Fe_3O_4 nanoparticles, (b) fabrication of the working glassy carbon electrode using glycine@Fe_3O_4, (c) glycine@Fe_3O_4-mediated DNA sensing, (d) DNA attracted towards the anode during DNA sensing through opposite charge attraction, and (e) interfering biomolecules attracted towards the cathode through opposite charge attraction.

this electrode and other positively charged interfering biomolecules present in the electrolyte may get attracted towards this electrode (Scheme 1e). Therefore, the present work is described as a non-enzymatic label-free DNA detection methodology with the help of glycine@Fe_3O_4 nanoparticles.

3.6. DNA sensing by computational analysis

Computational analysis was performed to support interactions between *K. pneumoniae* DNA and glycine molecules, as shown in Fig. 9a and b. Glycine, a simple chain amino acid, exhibits a property of cationic surface charge in an acidic environment. Chemically, it can be interpreted that cationic glycine and anionic DNA make a conjugate. However, glycine–DNA interactions were

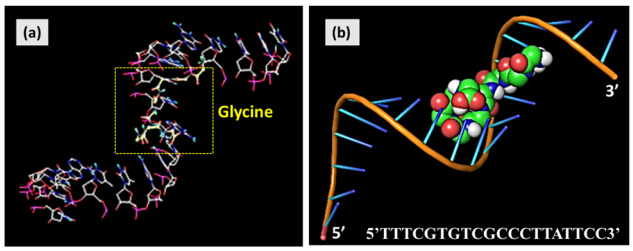

Fig. 9 Computational analysis of interactions between glycine and *K. pneumoniae* DNA. (a) DNA–glycine docking with PyRx 0.8, and (b) DNA–glycine conjugate visualization with Pymol.

seen to develop a bond or conjugate when studied computationally. Computer-aided interactions of different biomolecules are then predicted. A computational study (docking analysis) of the DNA–glycine conjugate was carried out using different software programs such as PyRx, Discovery studio 2021, Pymol, and so on. Docking analysis can be used for computational biology where possible bond formations are predicted when two biomolecules come in proximity. Here, DNA of *Klebsiella pneumoniae* and the glycine biomolecule were studied as a function of their conjugate formation. A DNA model was built by providing *Klebsiella pneumoniae* DNA sequence (5′TTTCGTGTCGCCCTTATTCC3′) using Discovery studio 2021. The protein data bank (PDB) model of glycine was taken from the PDB database. With PyRx 0.8, glycine and DNA macromolecule models were prepared for docking by minimizing their energy. These molecules were then docked. The docked image was directly obtained after the process was done as in Fig. 9a, where the glycine molecule was seen to be docked inside the DNA with a binding energy of around −6 kcal mol^{-1}. Negative binding energy provides natural binding interactions between molecules. The obtained model was visualized with Pymol software as shown in Fig. 9b. The figure clearly depicts the formation of the glycine–DNA conjugate.

4. Conclusions

This study presents a glycine-modified iron oxide (glycine@-Fe_3O_4) electrochemical biosensor for highly sensitive and selective detection of *Klebsiella pneumoniae* DNA, offering a rapid, cost-effective, and reliable alternative to conventional methods. The biosensor functions through label-free and non-enzymatic interactions, leveraging electrostatic attraction for efficient DNA binding.

Electrochemical characterization *via* CV, EIS, and SWV demonstrated DNA for the range 30–90 nM, LOD = 3.27 nM, R^2 = 0.9972, LOQ = 3.90 nM. For the higher range of 120–270 nM, LOD = 3.94 nM, R^2 = 0.9992, and LOQ = 11.95 nM, with a dynamic range of 0 to 300 nM, confirming high sensitivity. Sensitivity analysis revealed values of 1.441 μA nM^{-1} cm^{-2} for DNA, ensuring robust signal detection. Computational docking validated strong glycine–DNA binding interactions with a binding energy of approximately −6 kcal mol^{-1}, reinforcing the feasibility of the sensing mechanism. Selectivity tests confirmed negligible interference from whole bacterial cells,

proteins such as albumin, and bioanalytes including folic acid, ensuring accurate pathogen detection in complex biological samples. Clinical validation through PCR-based gel electrophoresis successfully identified key antimicrobial resistance genes SHV, TEM, CTX-M, and OXA-1, verifying the biosensor's real-world applicability for hospital infection surveillance.

This biosensor integrates high sensitivity, operational simplicity, and selectivity, making it an ideal candidate for point-of-care diagnostics and real-time infection monitoring. Future research should focus on expanding detection capabilities to other bacterial pathogens, validating performance with diverse clinical samples, and optimizing real-world implementation, further solidifying its role in combating antimicrobial resistance and hospital-acquired infections.

Data availability

The data supporting this article have been included as part of the ESI.†

Conflicts of interest

The authors declared no conflict of interest in the present work.

Acknowledgements

This work was supported by D. Y. Patil Education Society (Deemed to be University), Kolhapur through providing the required infrastructure, experimental facility, and financial support through an intramural project (No. DYPES/DU/R&D/2023/1164). This research work was also supported by Basic Science Research Program through the National Research Foundation of Korea (NRF) funded by the Ministry of Education (No. RS-2019-NR040081). The authors are thankful to the D. Y. Patil Hospital, Kolhapur, MS, India for gifting MDR *Klebsiella pneumoniae* cultures and the University of Madras, Chennai, India for helping with PCR validation. Dr T. D. Dongale and Prof. R. K. Kamat would like to thank RUSA Maharashtra for providing financial assistance under the 'RUSA-Industry Sponsored Centre for VLSI System Design'.

References

1 H. Namikawa, K. I. Oinuma, K. Yamada, Y. Kaneko, H. Kakeya and T. Shuto, Differences in severity of bacteremia caused by hypermucoviscous and non-hypermucoviscous Klebsiella pneumoniae, *Int. J. Antimicrob. Agents*, 2023, **61**(5), 106767.

2 C. L. Gorrie, M. Mirčeta, R. R. Wick, L. M. Judd, M. M. Lam, R. Gomi, I. J. Abbott, N. R. Thomson, R. A. Strugnell, N. F. Pratt and J. S. Garlick, Genomic dissection of Klebsiella pneumoniae infections in hospital patients reveals insights into an opportunistic pathogen, *Nat. Commun.*, 2022, **13**(1), 3017.

3 K. K. Tsang, M. M. Lam, R. R. Wick, K. L. Wyres, M. Bachman, S. Baker, K. Barry, S. Brisse, S. Campino, A. Chiaverini and D. M. Cirillo, Diversity, functional classification and genotyping of SHV β-lactamases in Klebsiella pneumoniae, *Microb. Genomics*, 2024, **10**(10), 001294.

4 P. Manohar, S. Leptihn, B. S. Lopes and R. Nachimuthu, Dissemination of carbapenem resistance and plasmids encoding carbapenemases in Gram-negative bacteria isolated in India, *JAC-Antimicrob. Resist.*, 2021, **3**(1), dlab015.

5 J. Henderson, H. Ciesielczuk, S. M. Nelson and M. Wilks, Community prevalence of carbapenemase-producing organisms in East London, *J. Hosp. Infect.*, 2019, **103**(2), 142–146.

6 A. Abuawad, Y. Ashhab, A. Offenhäusser and H. J. Krause, DNA Sensor for the Detection of Brucella spp. Based on Magnetic Nanoparticle Markers, *Int. J. Mol. Sci.*, 2023, **24**(24), 17272.

7 C. Tang, Z. He, H. Liu, Y. Xu, H. Huang, G. Yang, Z. Xiao, S. Li, H. Liu, Y. Deng and Z. Chen, Application of magnetic nanoparticles in nucleic acid detection, *J. Nanobiotechnol.*, 2020, **18**, 1–9.

8 G. Oza, K. Krishnajyothi, V. I. Merupo, K. A. Bracamontes, P. C. Olmos, E. Garrido, S. Velumani, M. Sridharan, A. Sharma, L. G. Arriaga and J. T. Ramirez, Gold-Iron oxide yolk-shell nanoparticles (YSNPs) as magnetic probe for fluorescence-based detection of 3 base mismatch DNA, *Colloids Surf., B*, 2019, **176**, 431–438.

9 C. Wan, A. Qu, M. Li, R. Tang, L. Fu, X. Liu, P. Wang and C. Wu, Electrochemical sensor for directional recognition and measurement of antibiotic resistance genes in water, *Anal. Chem.*, 2021, **94**(2), 732–739.

10 C. Wan, A. Qu, L. Deng, X. Liu and C. Wu, Preparation of electrochemical sensor based on glassy carbon electrode and its specificity and sensitivity for directional detection of antibiotic resistance genes spreading in the water environment, *Environ. Sci. Pollut. Res.*, 2023, **30**(3), 7904–7913.

11 K. Marchlewicz, I. Ostrowska, S. Oszwałdowski, A. Zasada, R. Ziółkowski and E. Malinowska, Molecular diagnostic of toxigenic Corynebacterium diphtheriae strain by DNA sensor potentially suitable for electrochemical point-of-care diagnostic, *Talanta*, 2021, **227**, 122161.

12 M. I. Hassan, K. R. Alkarshah, A. J. Alzarani, O. E. Obeied, A. H. Khamis and A. Diab, Detection of extended spectrum beta-lactamases-producing isolates and effect of AmpC overlapping, *J. Infect. Dev. Ctries.*, 2013, **7**(8), 618.

13 I. Carvalho, J. A. Carvalho, S. M. Alvarez, M. Sadi, R. Capita, C. A. Calleja, F. Rabbi, M. L. Dapkevicius, G. Igrejas, C. Torres and P. Poeta, Characterization of ESBL-producing Escherichia coli and Klebsiella pneumoniaeisolated from clinical samples in a northern Portuguese hospital: predominance of CTX-M-15 and high genetic diversity, *Microorganisms*, 2021, **9**(9), 1914.

14 C. S. S, V. Kini, M. Singh, C. Mukhopadhyay, P. Nag and K. Sadani, Disposable electrochemical biosensors for the detection of bacteria in the light of antimicrobial resistance, *Biotechnol. Bioeng.*, 2024, **121**(9), 2549–2584.

15 J. Wang, X. Cui, L. Liang, J. Li, B. Pang and J. Li, Advances in DNA-based electrochemical biosensors for the detection of foodborne pathogenic bacteria, *Talanta*, 2024, **275**, 126072.

16 M. Pan, Y. Zhao, J. Qiao and X. Meng, Electrochemical biosensors for pathogenic microorganisms detection based on recognition elements, *Folia Microbiol.*, 2024, **69**(2), 283–304.
17 A. G. da Silva Junior, I. A. Frias, R. G. Lima-Neto, O. L. Franco, M. D. Oliveira and C. A. Andrade, Electrochemical detection of Gram-negative bacteria through mastoparan-capped magnetic nanoparticle, *Enzyme Microb. Technol.*, 2022, **160**, 110088.
18 A. Khoshroo, M. Mavaei, M. Rostami, B. Valinezhad-Saghezi and A. Fattahi, Recent advances in electrochemical strategies for bacteria detection, *BioImpacts*, 2022, **12**(6), 567–588.
19 P. V. V. Romanholo, C. A. Razzino, P. A. Raymundo-Pereira, T. M. Prado, S. A. S. Machado and L. F. Sgobbi, Biomimetic electrochemical sensors: New horizons and challenges in biosensing applications, *Biosens. Bioelectron.*, 2021, **185**(1), 113242.
20 I. H. Cho, D. H. Kim and S. Park, Electrochemical biosensors: Perspective on functional nanomaterials for on-site analysis, *Biomater. Res.*, 2020, **24**(1), 1.
21 A. Villalonga, R. Villalonga and D. Vilela, Hybrid magnetic nanoparticles for electrochemical biosensors, *Magn. Nanopart.-Hybrid Mater.*, 2021, **1**(1), 679.
22 A. Sengupta, V. Sharma and B. Roy, Development of enzyme-based electrochemical biosensors: Advancements and limitations, *Biosensors*, 2025, **15**(3), 127.
23 R. Ahuja and N. Patel, Glycoprotein sensing through potentiometric methods: Challenges and innovations, *Sensors*, 2025, **25**(7), 2064.
24 H. Chen, Y. Liu and J. Zhou, Advances in DNA aptamer-based biosensors for electrochemical applications, *Lab Chip*, 2024, **15**(2), 67.
25 X. Zhang, L. Wang and J. Wei, Electrochemical analysis of protein biomarkers: A linear sweep voltammetry approach, *Biosensors*, 2023, **15**(3), 140.
26 S. Kumar and R. Gupta, Detection of RNA biomarkers using electrochemical techniques: Recent advancements, *Sensors*, 2023, **25**(5), 1212.
27 C. Lee and D. Han, Electrochemical glucose detection through amperometric biosensors, *Sensors*, 2022, **22**(4), 345.
28 T. Ahmed and M. Khan, Environmental applications of electrochemical sensors for heavy metal detection, *Sensors*, 2025, **25**(6), 2124.
29 N. Nagdeve and P. Kulkarni, miRNA biosensing using electrochemical techniques: Graphene-modified electrodes, *J. Biol. Eng.*, 2025, **14**(7), 98.
30 R. Singh and D. Chauhan, Pathogen detection using antibody-functionalized biosensors: EIS-based analysis, *SpringerLink*, 2024, **12**(3), 207.
31 D. Grieshaber and R. MacKenzie, Nanowire-based biosensors for enzyme detection: Opportunities and limitations, *Biosensors*, 2023, **13**(2), 187.
32 Q. Wang and Z. Zhang, DNA aptamer-functionalized electrochemical sensors: Advances in DPV and EIS techniques, *Sensors*, 2022, **15**(5), 92.
33 M. Patel and S. Kaur, Electrochemical biosensors for environmental toxin detection: Amperometric methodologies, *Sensors*, 2024, **20**(6), 287.
34 R. Lima and M. Pedro, Immunosensors for COVID-19 detection: Analytical performance and real-world applications, *Biosensors*, 2025, **15**(4), 300.
35 S. Varnakavi and H. Kim, Biomolecule detection using nanostructured materials: A review of SWV methods, *Sensors*, 2021, **22**(3), 1400.
36 A. Papreja and K. Saxena, *Enzyme-based biosensors for rapid electrochemical analysis: Cyclic voltammetry focus*, AIP Publ., 2023, vol. 45, 5, p. 78.
37 R. P. Gambhir, A. K. Parthasarathy, S. Sharma, S. Kale, V. V. Magdum and A. P. Tiwari, pH-responsive glycine functionalized magnetic iron oxide nanoparticles for SARS-CoV-2 RNA extraction from clinical sample, *J. Mater. Sci.*, 2022, **57**, 13620–13631.
38 P. C. Panta and C. P. Bergmann, Raman spectroscopy of iron oxide of nanoparticles (Fe_3O_4), *J. Mater. Sci. Eng.*, 2015, **5**(3), 1.
39 I. V. Krauklis, A. V. Tulub, A. V. Golovin and V. P. Chelibanov, Raman Spectra of Glycine and Their Modeling in Terms of the Discrete–Continuum Model of Their Water Solvation Shell, *Opt. Spectrosc.*, 2020, **128**(10), 1598.
40 C. Sudakar, P. Kharel, G. Lawes, R. Suryanarayanan, R. naik and V. M. Naik, Raman spectroscopic studies of oxygen defects in Co-doped ZnO films exhibiting room-temperature ferromagnetism, *J. Phys.: Condens. Matter*, 2006, **19**(2), 026212.
41 A. M. Abouzied, A. I. Al-falouji, S. I. Khalifa, H. T. Omran and H. A. Azab, Potential affinity binding of sarcophine to DNA, *Egypt. J. Nat. Toxins.*, 2007, **4**(1), 51.
42 A. Villalonga, R. Villalonga and D. Vilela, Hybrid magnetic nanoparticles for electrochemical biosensors, *Magn. Nanopart.-Hybrid Mater.*, 2021, **1**(1), 679.
43 Y. Yuan, F. Guillon, S. Griveau, F. Bedioui, M. Lazerges and C. Slim, Evolution of nucleic acids biosensors detection limit III, *Anal. Bioanal. Chem.*, 2022, **414**, 943–968.
44 M. Santhanam, I. Algov and L. Alfonta, DNA/RNA Electrochemical Biosensing Devices: A Future Replacement of PCR Methods for a Fast Epidemic Containment, *Sensors*, 2020, **20**(16), 4648.
45 G. Coletta and V. Amendola, Numerical Modelling of the Optical Properties of Plasmonic and Latex Nanoparticles to Improve the Detection Limit of Immuno-Turbidimetric Assays, *Nanomaterials*, 2021, **11**(5), 1147.
46 H. Wang, H. Wang, Y. Huang, H. Zhang, Y. Fu, Z. Yang, Y. Chen, X. Qiu, D. Yu and L. Zhang, Multi-parameter surface plasmon resonance instrument for multiple nucleic acid quantitative detection, *Biomed. Microdevices*, 2023, **25**, 1–24.
47 P. Vadhva, J. Hu, M. J. Johnson, R. Stocker, M. Braglia, D. J. L. Brett and A. J. E. Rettie, Electrochemical impedance spectroscopy for all-solid-state batteries: Theory, methods and future outlook, *ChemElectroChem*, 2021, **8**(11), 1930.